nature materials

ARTICLES

PUBLISHED ONLINE: 18 MAY 2015 | DOI: 10.1038/NMAT4288

Measuring surface dislocation nucleation in defect-scarce nanostructures

Lisa Y. Chen[1], Mo-rigen He[1], Jungho Shin[1], Gunther Richter[2] and Daniel S. Gianola[1]*

Linear defects in crystalline materials, known as dislocations, are central to the understanding of plastic deformation and mechanical strength, as well as control of performance in a variety of electronic and photonic materials. Despite nearly a century of research on dislocation structure and interactions, measurements of the energetics and kinetics of dislocation nucleation have not been possible, as synthesizing and testing pristine crystals absent of defects has been prohibitively challenging. Here, we report experiments that directly measure the surface dislocation nucleation strengths in high-quality ⟨110⟩ Pd nanowhiskers subjected to uniaxial tension. We find that, whereas nucleation strengths are weakly size- and strain-rate-dependent, a strong temperature dependence is uncovered, corroborating predictions that nucleation is assisted by thermal fluctuations. We measure atomic-scale activation volumes, which explain both the ultrahigh athermal strength as well as the temperature-dependent scatter, evident in our experiments and well captured by a thermal activation model.

The nearly century-long study of the structure and interactions of dislocations has been crucial for elucidating the properties and mechanical response of crystalline materials. Even before the invention of the transmission electron microscope (TEM), which facilitated direct observations of such defects[1], the concept of dislocations as a mechanism explaining the discrepancy between the theoretical strength in perfect crystals and the actual measured strength in real crystals had been proposed and developed[2–4]. The evidence of dislocations not only explained the ductile behaviour and work hardening abilities of metals relevant to structural applications for many centuries prior, but also informed other poorly understood phenomena in crystalline materials, such as rapid crystal growth[5], the facilitation of diffusion-less phase transformations[6], alloy corrosion[7], degradation of optoelectronic response[8], mobility enhancements in strained semiconductors[9], and solid-state amorphization in phase change devices[10].

Despite a rich understanding of the structure of dislocations pre-existing within crystals, their interactions with other defects, and even their annihilation, until recently it has been extremely challenging to address the details of the introduction—or nucleation—of dislocations in pristine crystals. In bulk crystals, the presence of pre-existing dislocations following synthesis or treatment is ubiquitous given the extreme conditions during crystal growth and relatively low energy barriers for nucleation, yet descriptions of their origin remain largely phenomenological. Nanostructured materials, on the other hand, can be synthesized with few or even zero defects, owing to the minuscule volumes of material and near-equilibrium crystal growth[11,12]. These materials, thus, operate in a regime where conventional dislocation processes are abated and must rely on nucleation to relieve large stresses and facilitate plastic deformation if brittle fracture is to be mitigated. As a large fraction of atoms in nanostructures resides at surfaces and interfaces, these materials are particularly prone to heterogeneous dislocation nucleation at ultrahigh stresses approaching the theoretical limit[12]. In these extreme settings, deformation mechanisms can be markedly different from their bulk counterparts[13–16].

Despite a relative scarcity of experiments able to directly observe or measure dislocation nucleation[12,17–23], several recent studies combining atomistic simulations and transition state theory (TST) have provided insight into the nucleation mechanism under various loading conditions[24–27]. These simulations and experiments all unequivocally show that ultrahigh stresses near the theoretical strength are required for the nucleation process in pristine crystals, with a value that is generally much less sensitive to specimen size than for micrometre-sized crystals[14,28]. Furthermore, nucleation is strongly assisted by thermal fluctuations with corresponding atomically small activation volumes, in stark contrast to bulk crystals. These predictions have been corroborated by systematic temperature-dependent nanoindentation studies of face-centred cubic (FCC) crystals, albeit in a complex state of loading with large stress gradients and a presumed location for nucleation[17,29].

A striking implication from the small activation volumes is an intrinsic thermal uncertainty[13,17,30] that in experiments or device operation would manifest as a pronounced stochasticity of nucleation strengths, collapsing to a singular strength only in the athermal limit (0 K). This necessitates a statistical approach to any study and demands a non-deterministic approach to device design. No experimental study, to our knowledge, exists that fully characterizes the temperature-, size- and strain-rate-dependent nucleation process, with quantifiable mechanistic, energetic and kinetic deliverables, in defect-scarce materials subjected to spatially uniform stress states. Such a study would bolster our understanding of dislocations in crystals in their most embryonic state—at the point of nucleation.

Here, we aim to address these fundamental questions and gain a quantitative description of the energetic and kinetic barriers to surface dislocation nucleation in pristine crystals. We present systematic experimental tensile tests performed on defect-scarce single-crystalline Pd nanowhiskers (NWs), where dislocation nucleation is the predominant mechanism underlying plastic yielding. We have probed the quasi-static tensile response over a range of strain rates, sizes and temperatures, even approaching the athermal limit. With the aid of *in situ* tensile tests in the

[1]Department of Materials Science and Engineering, University of Pennsylvania, Philadelphia, Pennsylvania 19104, USA. [2]Max-Planck-Institut für Intelligente Systeme, D-70589 Stuttgart, Germany. *e-mail: gianola@seas.upenn.edu

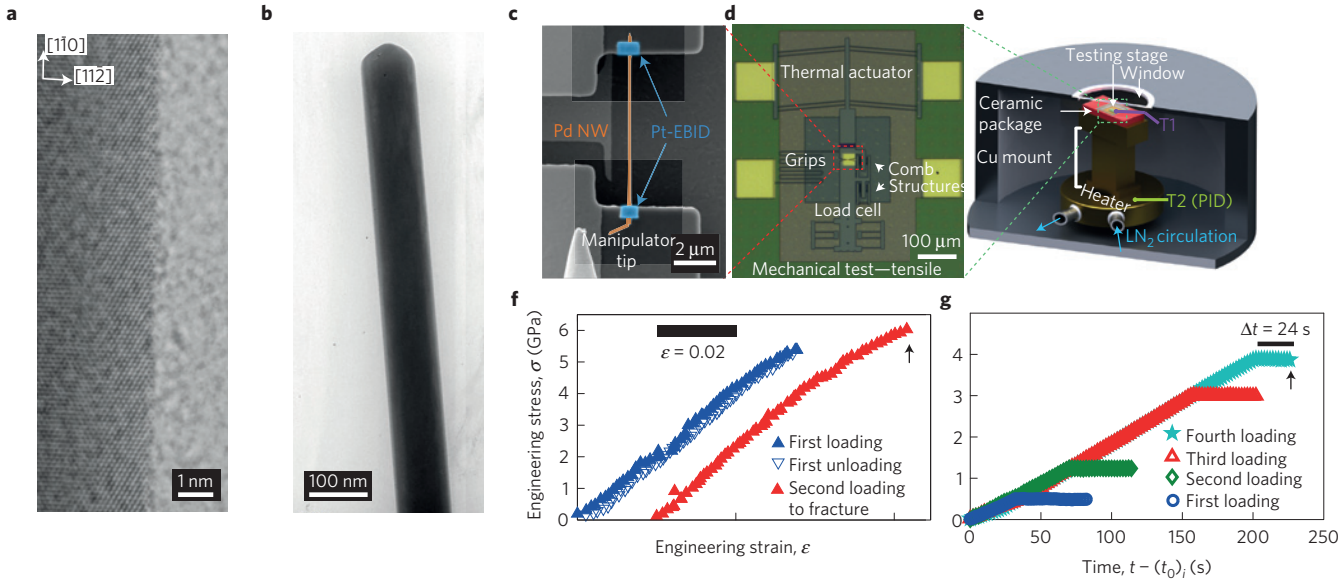

Figure 1 | Experimental method and verification of elasticity. a, High-resolution TEM micrograph of the surface morphology of a Pd NW along an edge between two facets. **b**, Bright-field TEM micrograph of a Pd NW. **c**, SEM micrograph of an individually manipulated NW mounted to the tensile testing stage grips. NW and EBID grips are artificially coloured for clarity. **d**, Optical micrograph of the MEMS tensile testing stage. **e**, Temperature testing configuration in the cryostat with the MEMS stage mounted in a ceramic package. A thermocouple mounted on the MEMS chip (T1) provides the sample temperature, and a Si diode sensor at the heat exchange base (T2) provides the reading to a PID temperature controller. **f**, Sample load–unload and subsequent fracture stress–strain curves for a single Pd NW, offset for clarity. **g**, Load-hold tests performed on a Pd NW to verify elasticity at high stresses. Time along the abscissa is with respect to the start time $(t_0)_i$ of the ith loading. Fractures in **f**,**g** occur where indicated by the black arrows.

TEM, we demonstrate a direct connection between incipient plasticity in our NWs and the nucleation of dislocations at free surfaces. Our measurements of over 60 individual NWs provide values for the energy barriers and kinetics governing dislocation nucleation, as well as insight into the highly probabilistic nature of dislocation nucleation.

Ultrahigh strength due to surface dislocation nucleation

The Pd NWs in this study are of high crystalline quality and defect-scarce owing to near-equilibrium growth conditions. Whereas no pre-existing unit dislocations were observed in any of our TEM investigations, a fraction of NWs from certain growth substrates contained a stacking fault along the axis of the NW, which is not expected to contribute to plastic deformation (see Methods and Supplementary Information). Individual specimens (Fig. 1a,b) were tested in tension using the set-up shown in Fig. 1c–e. Beginning with room temperature tensile behaviour, the Pd NWs exhibited large ultimate strengths as high as 7.8 GPa, over 200 times stronger than their bulk counterparts. In all Pd NWs tested, the elastic response became nonlinear at strains above 1% (ref. 31). Elastic deformation was confirmed by performing a series of load–unload tests to increasingly high strains, where on unloading the curve follows a nonlinear path back to zero load and strain (Fig. 1f). The elastic regime was terminated at strengths near the theoretical limit of Pd (ref. 32) by fracture or, in only four cases, a clearly distinguishable plastic flow regime in which the load remained approximately constant (see Supplementary Fig. 2). Additional load-hold testing provided further evidence of sustained elasticity and the absence of relaxation mechanisms at stresses well below the yield or fracture strengths. Figure 1g shows subsequent loadings of a single NW, which sustained a relatively constant load at increasingly higher levels of stress until fracture occurred during the final holding period. The finite duration of time (~24 s at 3.8 GPa) required for yield to occur under constant stress is consistent with a thermally activated mechanism and can be related to the expectation time for the first nucleation event.

The measured stress–strain response in our Pd NWs suggests that defect nucleation, and thus plastic deformation, is associated with the first measured deviations from elasticity. However, *in situ* TEM tests performed on other metallic nanostructures with non-zero defect density have shown that dislocation motion may still occur during what would otherwise seem to be elastic loading[33]. To verify the absence of dislocation motion or nucleation before yield or departure from elasticity in the stress–strain curve, we performed quantitative *in situ* TEM tensile tests on the Pd NWs.

Figure 2b–e shows a series of images captured during tensile testing of a Pd NW with a diameter of 60 nm, and Fig. 2f shows the corresponding stress–strain curve, which is described well by a nonlinear (quadratic) elastic relationship before fracture, as reported previously[31]. For this NW, diffraction contrast related to defects, such as dislocations and stacking faults, was not observed at the beginning of the test (Fig. 2b). Moreover, the NW remained defect-free during the test, for example, near the onset of nonlinear elasticity (Fig. 2c) and before the NW fractured (Fig. 2d) at a stress of 3.45 GPa. Subsequently, the NW abruptly fractured (Fig. 2e) in a shear mode (see Fig. 2g), with a shear plane determined to be $(1\bar{1}1)$, as the NW was oriented along $[1\bar{1}0]$ and observed in the [110] zone axis. Traces of stacking faults were observed parallel to the major $(1\bar{1}1)$ shear plane (and the equivalent $(\bar{1}11)$ plane), indicating that the shear fracture probably occurred by activation of a series of identical partial dislocations with $\mathbf{b}=[\bar{1}12]a/6$ (and the equivalent $\mathbf{b}=[1\bar{1}2]a/6$) from the side surfaces, which accorded well with previous atomistic simulations and *in situ* scanning electron microscope (SEM) measurements of Au NWs (ref. 34). Notably, no visible surface steps were evident during or after loading away from the fracture edge, which could arise from dislocation avalanches operating at speeds faster than our video rate. Figure 2h,i shows the stress–strain curve and fracture morphology of another defect-free Pd NW with a diameter of 64 nm, which was elastically loaded to 6.7 GPa and then fractured in a necking-like mode. Traces of stacking faults (or twinning planes) were also observed only near the fracture edges. A Schmid factor

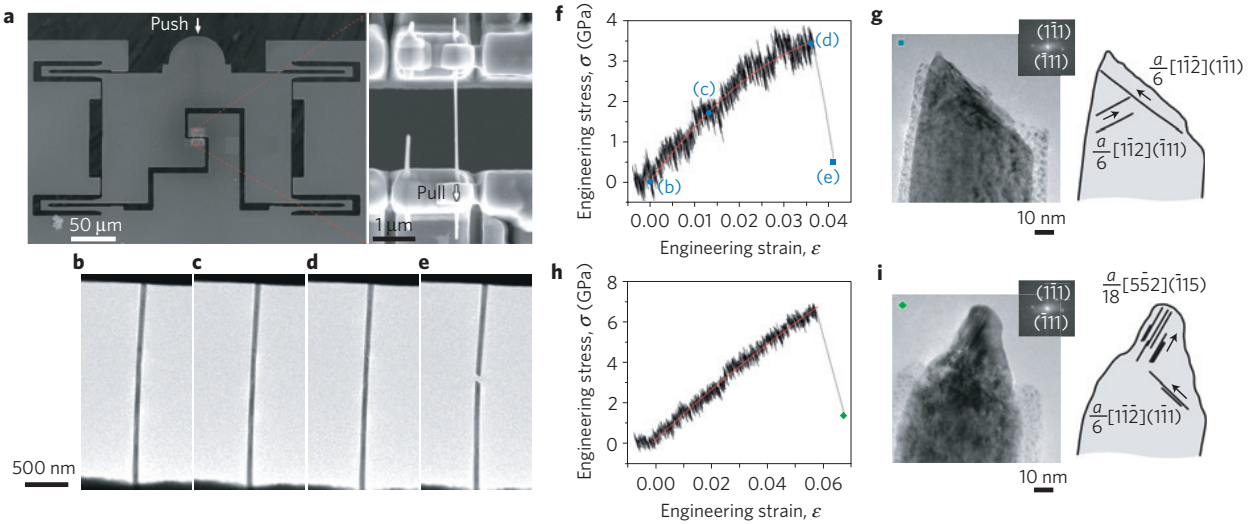

Figure 2 | *In situ* TEM tensile testing shows dislocation nucleation and failure occurring in short succession. a, Push-to-pull device with a secured NW. **b**–**e**, Sequential images from a single tensile test on a Pd NW. **f**, Stress–strain curve with a quadratic fit for the nonlinear response (red line) corresponding to the sequence in **b**–**e**. **g**, Fracture morphology showing stacking faults from equivalent slip systems. **h**, A second Pd NW of similar diameter tested under identical conditions. **i**, Fracture morphology of the second NW, showing sequential twinning on different slip systems. **g**,**i** were taken atomically resolved in high-resolution TEM mode parallel to the [110] crystal direction of Pd; the insets depict the fast Fourier transform (FFT) of the fracture areas respectively. The stacking fault planes are parallel and edge-on to the electron beam. No moiré patterns are observed that would evidence the presence of other stacking faults inclined to the electron beam. Detailed analyses of the observed slip plane traces can be found in the Supplementary Information.

analysis (see Supplementary Information) suggested that plastic deformation in this NW was mediated by partial dislocations (or twinning segments), operating in a primary slip system with $\mathbf{b}=[\bar{1}12]a/6$ on a $(1\bar{1}1)$ plane, followed by a secondary system with $\mathbf{b}=[5\bar{5}2]a/18$ on a $(\bar{1}15)$ plane with respect to the matrix orientation, which is equivalent to $\mathbf{b}=[1\bar{1}2]a/6$ on the $(\bar{1}11)$ plane in the primary twinned region. Such a plasticity mechanism mediated by multiple partial dislocations is consistent with previous studies of Au NWs grown in similar conditions[34], underscoring the role of dislocation nucleation from the surface of these NWs.

Our *in situ* TEM testing revealed that mobile dislocations were present neither inside the Pd NWs before testing nor during the entirety of the evidently elastic regime. However, clear evidence of late-stage plastic deformation strongly suggests that nucleation of dislocations gives rise to highly localized plastic deformation, followed rapidly by final fracture. Thus, the yield strengths measured in this study serve as a reasonable indicator of incipient plasticity and can be used for evaluating the critical stress for dislocation nucleation.

Effect of experimental parameters on nucleation

Probing the dependence of nucleation strength on testing parameters such as size, strain rate and temperature provided further quantitative insight to the underlying plasticity mechanism. To minimize convolution in the data, we define our benchmark conditions as NWs tested at room temperature (295 K) and an intermediate strain rate range ($\sim 10^{-4}\ s^{-1}$)—that is, all non-ambient temperature tests were performed at a strain rate in the $10^{-4}\ s^{-1}$ range and all tests performed above or below $10^{-4}\ s^{-1}$ were at room temperature. In Fig. 3, several characteristics of the tensile response, including ultrahigh yield strength in the gigapascal range and nonlinear elasticity at high strains, remain consistent among the different testing conditions. Elasticity at high strengths was again verified by performing load–unload tests before the fracture (see Supplementary Fig. 1).

Our results reveal the following trends for the nucleation strength. At room temperature, changes of two orders of magnitude in strain rate do not produce significant differences in the yield strengths. In contrast, spanning a temperature range of ~300 K demonstrates significant changes in yield strength. For the tensile test performed at 93 K, a yield strength as high as 5.8 GPa was attained. In contrast, the sample tested at 447 K fractured at a much lower strength of 2.8 GPa. This strong temperature dependence points to a deformation mechanism more thermally sensitive than the flow of pre-existing dislocations in FCC crystals[35], the strength for which would scale only weakly with the elastic constants (~4% versus 50% drop in strength for the given temperature range, for bulk and Pd NWs, respectively). Similar to the *in situ* TEM tests, the measured tensile response indicates a brittle-like behaviour whereas the fracture surface suggests otherwise. Fracture morphologies on all specimens indicate localized necking or shear deformation consistent with the previous *in situ* tests (Fig. 3c–g), suggesting that dislocation mechanisms govern plastic deformation over the entire range of tested strain rates and temperatures.

The experimental trends measured and illustrated in Fig. 3 are qualitatively consistent with theoretical predictions, both from semi-analytical models[26,36] and computational simulations[27,36,37], where strength is weakly dependent on strain rate but strongly dependent on temperature. The stochasticity of the measured nucleation strengths spanning several GPa under benchmark conditions for instance (Fig. 4), however, adds a statistical facet to the mechanism. Examining the measured strength as a function of size, either represented as diameter (Fig. 4a) or gauge length (Fig. 4b), shows a marginal size effect relative to this scatter over the tested range. This observation is likewise consistent with predictions[26,36] and other experiments[12,26] indicating weak size effects in defect-free metallic nanostructures. To determine the origin of the large scatter in measured strengths, we first systematically consider sources of experimental uncertainty, including effects such as variation in the applied strain rate, estimation of the cross-sectional area, and load bearing by a hydrocarbon-based contamination layer. We also consider any correlation of measured strength with fracture location and with the presence of the axially aligned stacking faults. As detailed in the Supplementary Information and indicated by error bars on our data, these cumulative uncertainties are substantially smaller than the measured scatter. We therefore attribute the stochasticity of

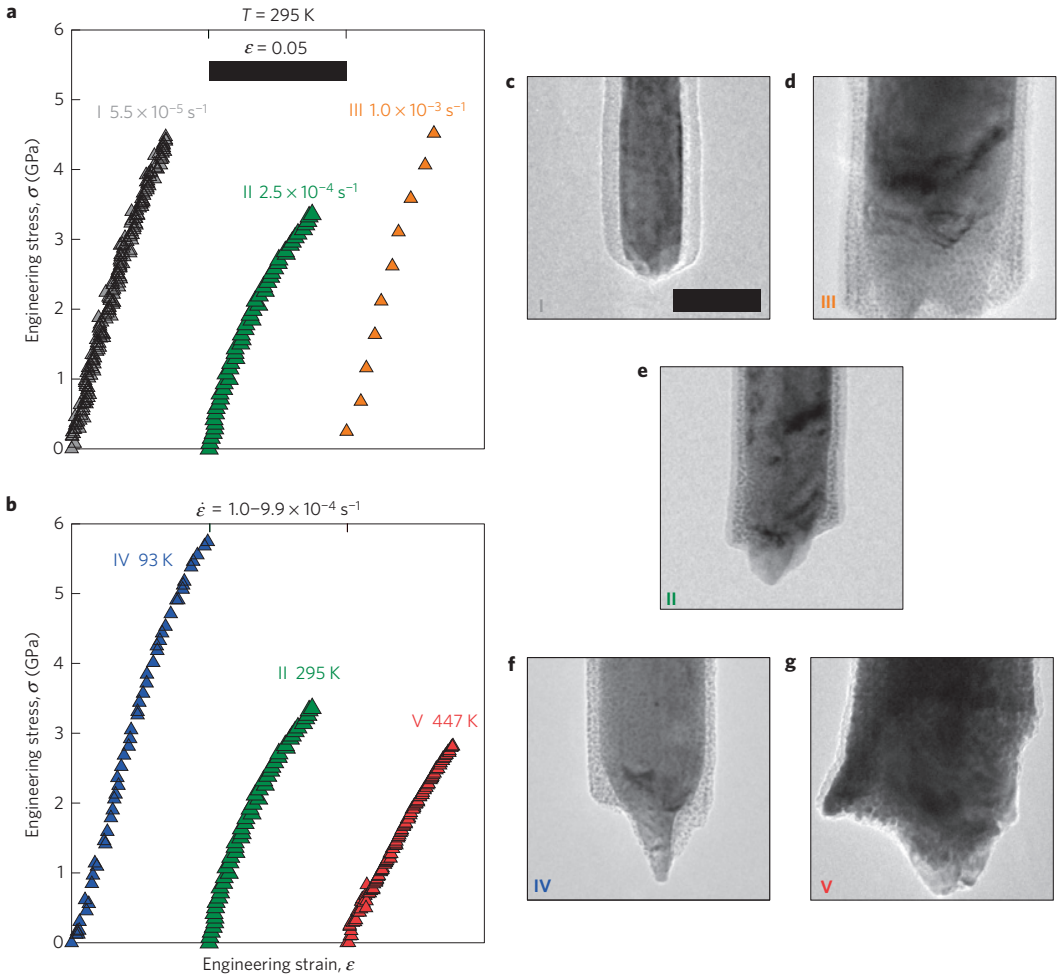

Figure 3 | Representative stress–strain behaviour shows strong temperature dependence of the nucleation strength and a similar deformation morphology irrespective of testing conditions. a,**b**, Stress–strain curves for tensile tests performed under various strain rate (**a**) and temperature (**b**) conditions. Stress-strain curves are offset for clarity with the strain quantity indicated by the bar in **a**. **c**–**g**, Corresponding postmortem fracture morphologies for the tensile tests labelled I–V in **a**,**b**. The nonlinear elastic response leading up to the nucleation event was found to be size-dependent in both the small strain (Young's) and higher order moduli owing to the increasing contribution of surface stresses with diminishing size coupled with the large lattice anharmonicity of Pd (ref. 31). All fracture micrographs are at the same magnification and correspond to the scale bar in **c** denoting 50 nm. We note that only fractured samples in IV (**f**) and V (**g**) are from the respective non-ambient temperature tests in **b**, but samples I (**c**), II (**e**) and III (**d**) were tested under the same conditions as the corresponding tests shown in **a**. The hydrocarbon-based coatings are the result of NW manipulation before and after tensile testing; a detailed analysis of its influence is presented in the Supplementary Information.

our measurements to a probabilistic thermally activated deformation process.

Examining the full data set of over 60 NWs, we find that whereas tensile tests performed at various strain rates do not show a rate dependence that rises above the scatter (Fig. 5a), the nucleation strength is found to vary significantly with temperature. Comparing the mean strength values at the tested temperature limits shows a strength reduction of nearly 6 GPa over a 350 K increase in temperature (Fig. 5b). This large monotonic decrease in strength with increasing temperature, associated with dislocation-mediated deformation, unambiguously points to a thermally activated process. As well as the mean strength, the measured scatter band is also a function of temperature, with the largest variation emerging near room temperature and reducing in both the athermal (with thermal fluctuations absent) and high-temperature (bounded by zero stress) limits.

Discussion and theoretical comparisons

We analyse these temperature-dependent distributions of nucleation strength to evaluate the thermal activation parameters associated with surface dislocation nucleation. From TST, the rate of dislocation nucleation ν is expressed as:

$$\nu = N\nu_0 \exp\left(-\frac{\Delta G_{act}(\sigma,T)}{k_B T}\right) \quad (1)$$

where ν_0 is the attempt frequency, N is the number of equivalent nucleation sites, $\Delta G_{act}(\sigma,T)$ is the activation free energy and k_B is the Boltzmann constant. To directly compare our experimental results against the proposed temperature and stress dependencies of ΔG_{act}, we adopt the simple form for the activation energy following the work of refs 36–38:

$$\Delta G_{act}(\sigma,T) = \Delta U_{act}\left(1-\frac{T}{T_m}\right)\left(1-\frac{\sigma}{\sigma_{ath}}\right)^{\alpha} \quad (2)$$

Here, σ_{ath} is the athermal strength, ΔU_{act} is the zero-temperature, zero-stress activation energy, and both T_m and α are constants governing the temperature and stress dependencies, respectively[36]. Mechanistically, α is related to the particular obstacle that must be overcome during the thermally activated process. A strong stress dependence has been proposed ($\alpha \approx 4$) on the

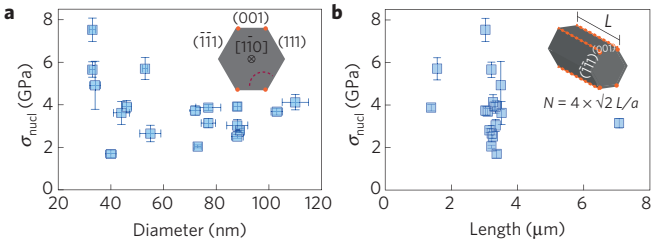

Figure 4 | Weak size dependence of nucleation strength. a,**b**, Nucleation strengths measured in Pd NWs across a range of diameters (**a**) and gauge lengths (**b**) at $T = 295$ K and strain rates of the order of 10^{-4} s^{-1}. Schematics in the upper right-hand corners illustrate predicted nucleation of a dislocation from a corner site in **a** and the relationship between length L and number of equally viable nucleation sites N for lattice parameter a in **b**. Viable nucleation sites are indicated by orange circles or orange dotted lines. Horizontal error bars in **a** correspond to the standard deviation of at least ten measurements of diameter; the length of each sample was measured only once, so there are no horizontal error bars in **b**. Vertical error bars in **a**,**b** were calculated from the uncertainties in cross-section (diameter) and load measurements. See Supplementary Information for more details.

basis of calculations of the activation energy for simulations of heterogeneous corner dislocation nucleation in a Cu NW under tension[36]. We thus compute the full temperature-dependent nucleation strength distributions for both $\alpha = 1$ (as has been assumed for dislocation nucleation in refs 30,39) and $\alpha = 4$ to draw comparisons to our experiments (for details of these derivations, see the Supplementary Information).

We employ the approach taken in ref. 40, and substitute equation (2) for $\alpha = 4$ into equation (1) to define a cumulative probability distribution function $F(\sigma)$ (Supplementary Equations 4 and 7); we fit this to the experimental data to obtain σ_{ath}, the Arrhenius prefactor $N\nu_0$, and the Helmholtz free energy of activation $\Delta F_{act}(T) = \Delta U_{act}(1 - T/T_m)$ (Fig. 5c). Using nonlinear least squares regression, we obtain $\sigma_{ath} = 7.08 \pm 0.02$ GPa, $N\nu_0 = 0.065 \pm 0.003$ s^{-1}, and $\Delta F_{act}(T) = 0.236 \pm 0.009$ eV. Assuming T_m is half the bulk melting temperature of Pd ($T_m = 914$ K), we then calculate $\Delta U_{act} = 0.328$ eV.

Using these values, we calculate the most probable critical nucleation strength σ_c at 295 K for $\alpha = 4 (\alpha = 1)$ to be 3.44 GPa (5.85 GPa), which corresponds to an activation energy and volume $\Delta G_{act} = 0.016$ eV$(0.048$ eV$)$ and $\Omega = 2.70$ Å$^3 = 0.13b^3 (4.79$ Å$^3)$, respectively, where b is the magnitude of the full FCC Burgers vector. In comparison, simulations of surface dislocation nucleation in a Cu NW in tension yield $\Delta G_{act} = 0.39$ eV and $\Omega = 5b^3$ at the same temperature and fraction of the athermal strength[36], at least an order of magnitude higher than those from our experiments on Pd NWs. Likewise, our calculated maximum activation entropy for Pd is $4.17k_B$, implying a non-negligible contribution to the nucleation rate ($\sim \exp(\Delta S_{act}/k_B)$). This compares with calculations giving $9k_B$ and $48k_B$ for homogeneous nucleation in Cu under constant strain and stress, respectively[27]. Considering the low activation energies deduced from our experiments, it is plausible that certain pre-existing flaws that go undetected, such as vacancies and atomic surface steps, could lower the nucleation barrier with respect to an ideal crystal. In Pd, the vacancy migration energy is reported as 0.82 eV, and the formation energy and volumes as 1.4 eV and $0.24b^3$, respectively[41]; given these larger barriers, it is unlikely that they contribute significantly to the experimentally observed behaviour. On the other hand, surface self-diffusion on {111} Pd facets (predominant on the surfaces of our NW specimens) has an activation energy of 0.031 eV (ref. 42), comparable to the energy we measure and consistent with an atomically sized activation volume. The striking implication is, thus, that surface diffusion, mediated by stresses near the ideal limit, may serve as a precursor mechanism to displacive ones that produce dislocation content within the crystal[15]. This notion is also consistent with recent observations of stress-assisted plastic deformation in Ag nanoparticles, where diffusive plasticity led to large pseudoelastic response[16]. In addition, pre-existing flaws such as surface steps are plausible in experimental specimens: simulation studies have shown that the activation parameters for nucleation can change significantly in the presence of such defects[36,43]. Their role, however, hinges on the configuration of these flaws relative to the applied stress and other defects. For instance, simulations of kinks on existing surface steps were shown not to influence the elastic limit in Al (ref. 43). Ultimately, the contributions from intrinsic (thermal fluctuations) and extrinsic (variations in surface quality from specimen to specimen) stochasticity could presumably be discerned by testing at even lower temperatures near 0 K; thus, the activation parameters we report here are effective ones.

The probabilistic nature of surface dislocation nucleation instantly emerges when comparing our full data set with computed temperature-dependent probability distribution function (PDFs). The PDF at each temperature is shown in Fig. 6 and normalized by its maximum probability to highlight the trajectory of σ_c over temperature. We compare our data against cases of both strong

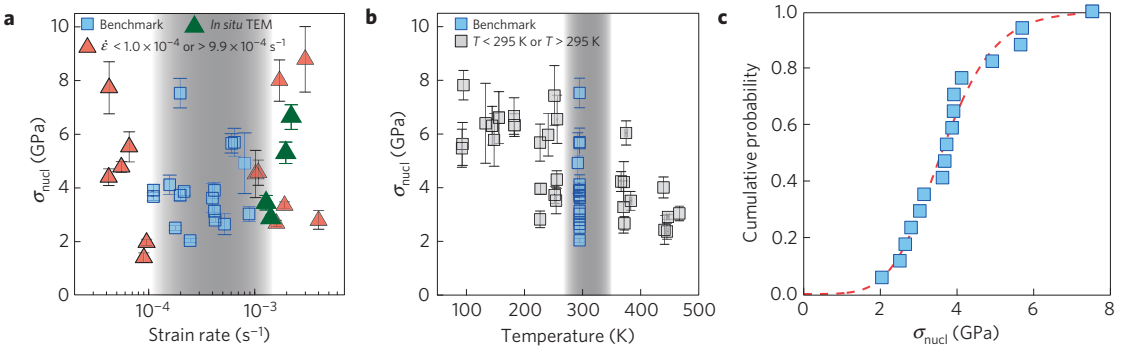

Figure 5 | Strain rate and temperature dependence, and statistical analysis of benchmark experiments. a,**b**, Nucleation strength in Pd NWs measured for different strain rates (**a**)—including results from the *in situ* TEM tests (green triangles)—and different temperatures (**b**). Blue squares and grey shading represent measurements at 295 K and strain rates of the order of 10^{-4} s^{-1}, as shown in Fig. 4. Measurements outside of these benchmark conditions are indicated by a different colour or symbol (triangles for strain rate outside 10^{-4} s^{-1}, black and grey for T outside 295 ± 5 K). Vertical error bars in **a**,**b** were calculated from the uncertainties in cross-section (diameter) and load measurements. See Supplementary Information for more details. **c**, Cumulative probability for measured yield strengths. The dotted red line is a fit for the analytically derived cumulative distribution function $F(\sigma)$.

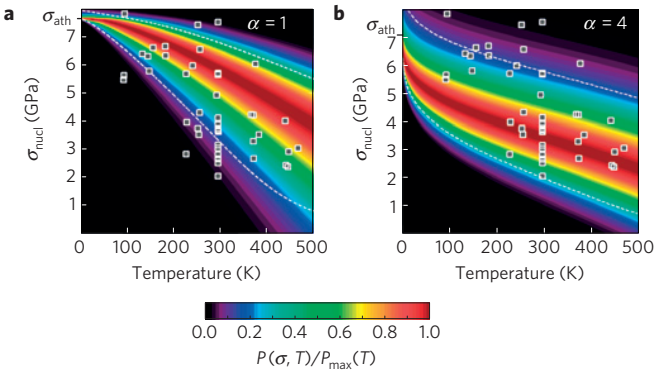

Figure 6 | Comparison between the experimental temperature-dependent nucleation strength distribution and the analytical model for the probability distribution. a,**b**, Normalized PDF maps for $\alpha = 1$ (**a**) and $\alpha = 4$ (**b**) are overlaid with measured nucleation stress (grey squares) at strain rates of the order of 10^{-4} s^{-1} (data points same as in Fig. 5b). The respective values for σ_{ath} are indicated on the vertical axes. Probability values $P(\sigma, T)$ are normalized with respect to the maximum probability $P_{max}(T)$ at each temperature; thus, each vertical slice represents the probability distribution at a given temperature, which collapses to a deterministic value in the athermal limit. The dashed contour lines represent the 5th (lower) and 95th (upper) percentile nucleation stresses.

($\alpha = 4$) and weak ($\alpha = 1$) stress dependence of the activation energy. Both models capture the strong temperature dependence of the mean nucleation strength and, more remarkably, of the non-monotonic scatter in probable nucleation strengths observed in experiment. Contour lines indicating the 5th and 95th percentile nucleation strength at each temperature show that the influence of α is most evident at low temperatures, particularly in the athermal limit, suggesting that further measurements at ultralow temperatures would be a promising avenue to gain further insight into the details of surface nucleation.

In summary, we have quantified the energetic and kinetic barriers to surface dislocation nucleation-mediated plastic deformation in uniformly strained NWs. Our results provide new insight into a class of defects that affect material properties and device performance in a host of technological sectors. We find that the plastic deformation is mediated by surface dislocation nucleation at ultrahigh stresses (athermal strength ~8% of the shear modulus) near the theoretical limit of strength, representing the highest ever measured in an FCC metal. Our experiments uncover a strong temperature dependence of strength and its associated scatter, well in excess of what is observed in bulk FCC metals and suggesting a surface diffusion mechanism as the rate-limiting step needed to promote displacive activity. Our results can ultimately be used to predict the nucleation behaviour under extreme conditions and inform probabilistic models and device design strategies employing nanoscale materials.

Methods

Methods and any associated references are available in the online version of the paper.

Received 20 February 2015; accepted 2 April 2015; published online 18 May 2015

References

1. Hirsch, P. B., Horne, R. W. & Whelan, M. J. LXVIII Direct observations of the arrangement and motion of dislocations in aluminium. *Phil. Mag.* **1,** 677–684 (1956).
2. Taylor, G. I. The mechanism of plastic deformation of crystals. Part I. Theoretical. *Proc. R. Soc. Lond. A* **145,** 362–387 (1934).
3. Orowan, E. Zur Kristallplastizität. I. *Z. Phys.* **89,** 605–613 (1934).
4. Polanyi, M. Über eine Art Gitterstörung, die einen Kristall plastisch machen könnte. *Z. Phys.* **89,** 660–664 (1934).
5. Frank, F. C. The influence of dislocations on crystal growth. *Discuss. Faraday Soc.* **5,** 48–54 (1949).
6. Hirth, J. P. & Pond, R. C. Steps, dislocations and disconnections as interface defects relating to structure and phase transformations. *Acta Mater.* **44,** 4749–4763 (1996).
7. Swann, P. R. Dislocation substructure vs transgranular stress corrosion susceptibility of single phase alloys. *Corrosion* **19,** 102t–114t (1963).
8. Farvacque, J. L., Douehan, J. C., von Alpen, U. & Gmelin, E. Screw-dislocation-induced scattering processes and acceptor states in Te. *Phys. Status Solidi* **79,** 763–773 (1977).
9. Lee, M. L., Fitzgerald, E. A., Bulsara, M. T., Currie, M. T. & Lochtefeld, A. Strained Si, SiGe, and Ge channels for high-mobility metal-oxide-semiconductor field-effect transistors. *J. Appl. Phys.* **97,** 011101 (2005).
10. Nam, S-W. *et al.* Electrical wind force-driven and dislocation-templated amorphization in phase-change nanowires. *Science* **336,** 1561–1566 (2012).
11. Wagner, R. S. & Ellis, W. C. Vapor–liquid–solid mechanism of single crystal growth. *Appl. Phys. Lett.* **4,** 89–90 (1964).
12. Richter, G. *et al.* Ultrahigh strength single crystalline nanowhiskers grown by physical vapor deposition. *Nano Lett.* **9,** 3048–3052 (2009).
13. Zhu, T. & Li, J. Ultra-strength materials. *Prog. Mater. Sci.* **55,** 710–757 (2010).
14. Greer, J. R. & De Hosson, J. T. M. Plasticity in small-sized metallic systems: Intrinsic versus extrinsic size effect. *Prog. Mater. Sci.* **56,** 654–724 (2011).
15. Li, J. *et al.* Diffusive molecular dynamics and its application to nanoindentation and sintering. *Phys. Rev. B* **84,** 054103 (2011).
16. Sun, J. *et al.* Liquid-like pseudoelasticity of sub-10-nm crystalline silver particles. *Nature Mater.* **13,** 1007–1012 (2014).
17. Schuh, C. A., Mason, J. K. & Lund, A. C. Quantitative insight into dislocation nucleation from high-temperature nanoindentation experiments. *Nature Mater.* **4,** 617–621 (2005).
18. Oh, S. H., Legros, M., Kiener, D. & Dehm, G. *In situ* observation of dislocation nucleation and escape in a submicrometre aluminium single crystal. *Nature Mater.* **8,** 95–100 (2009).
19. Zheng, H. *et al.* Discrete plasticity in sub-10-nm-sized gold crystals. *Nature Commun.* **1,** 144 (2010).
20. Jennings, A. T., Li, J. & Greer, J. R. Emergence of strain-rate sensitivity in Cu nanopillars: Transition from dislocation multiplication to dislocation nucleation. *Acta Mater.* **59,** 5627–5637 (2011).
21. Lu, Y., Song, J., Huang, J. Y. & Lou, J. Surface dislocation nucleation mediated deformation and ultrahigh strength in sub-10-nm gold nanowires. *Nano Res.* **4,** 1261–1267 (2011).
22. Bei, H., Gao, Y., Shim, S., George, E. & Pharr, G. Strength differences arising from homogeneous versus heterogeneous dislocation nucleation. *Phys. Rev. B* **77,** 060103 (2008).
23. Gerberich, W. W., Nelson, J. C., Lilleodden, E. T., Anderson, P. & Wyrobek, J. T. Indentation induced dislocation nucleation: The initial yield point. *Acta Mater.* **44,** 3585–3598 (1996).
24. Li, J., Van Vliet, K. J., Zhu, T., Yip, S. & Suresh, S. Atomistic mechanisms governing elastic limit and incipient plasticity in crystals. *Nature* **418,** 307–310 (2002).
25. Warner, D. H. & Curtin, W. A. Origins and implications of temperature-dependent activation energy barriers for dislocation nucleation in face-centered cubic metals. *Acta Mater.* **57,** 4267–4277 (2009).
26. Jennings, A. T. *et al.* Modeling dislocation nucleation strengths in pristine metallic nanowires under experimental conditions. *Acta Mater.* **61,** 2244–2259 (2013).
27. Ryu, S., Kang, K. & Cai, W. Entropic effect on the rate of dislocation nucleation. *Proc. Natl Acad. Sci. USA* **108,** 5174–5178 (2011).
28. Uchic, M. D., Dimiduk, D. M., Florando, J. N. & Nix, W. D. Sample dimensions influence strength and crystal plasticity. *Science* **305,** 986–989 (2004).
29. Bahr, D. F., Wilson, D. E. & Crowson, D. A. Energy considerations regarding yield points during indentation. *J. Mater. Res.* **14,** 2269–2275 (2011).
30. Ngan, A. H. W., Zuo, L. & Wo, P. C. Size dependence and stochastic nature of yield strength of micron-sized crystals: A case study on Ni3Al. *Proc. R. Soc. Lond. A* **462,** 1661–1681 (2006).
31. Chen, L., Richter, G., Sullivan, J. & Gianola, D. Lattice anharmonicity in defect-free Pd nanowhiskers. *Phys. Rev. Lett.* **109,** 125503 (2012).
32. Kamran, S., Chen, K. & Chen, L. *Ab initio* examination of ductility features of fcc metals. *Phys. Rev. B* **79,** 024106 (2009).
33. Chisholm, C. *et al.* Dislocation starvation and exhaustion hardening in Mo alloy nanofibers. *Acta Mater.* **60,** 2258–2264 (2012).
34. Sedlmayr, A. *et al.* Existence of two twinning-mediated plastic deformation modes in Au nanowhiskers. *Acta Mater.* **60,** 3985–3993 (2012).

35. Masumoto, H., Saitô, H. & Kadowaki, S. Young's modulus of single crystals of palladium at high temperatures. *Sci. Rep. Res. Inst. Tohoku Univ. A* **19,** 294–303 (1967).
36. Zhu, T., Li, J., Samanta, A., Leach, A. & Gall, K. Temperature and strain-rate dependence of surface dislocation nucleation. *Phys. Rev. Lett.* **100,** 025502 (2008).
37. Ryu, S., Kang, K. & Cai, W. Predicting the dislocation nucleation rate as a function of temperature and stress. *J. Mater. Res.* **26,** 2335–2354 (2011).
38. Kocks, U. F., Argon, A. & Ashby, M. F. *Thermodynamics and Kinetics of Slip* (Argonne National Laboratory, 1973).
39. Mason, J., Lund, A. & Schuh, C. Determining the activation energy and volume for the onset of plasticity during nanoindentation. *Phys. Rev. B* **73,** 054102 (2006).
40. Zuo, L. & Ngan, A. H. W. Molecular dynamics study on compressive yield strength in Ni_3Al micro-pillars. *Phil. Mag. Lett.* **86,** 355–365 (2006).
41. Foiles, S., Baskes, M. & Daw, M. Embedded-atom-method functions for the fcc metals Cu, Ag, Au, Ni, Pd, Pt, and their alloys. *Phys. Rev. B* **33,** 7983–7991 (1986).
42. Liu, C. L., Cohen, J. M., Adams, J. B. & Voter, A. F. EAM study of surface self-diffusion. *Surf. Sci.* **253,** 334–344 (1991).
43. Brochard, S., Hirel, P., Pizzagalli, L. & Godet, J. Elastic limit for surface step dislocation nucleation in face-centered cubic metals: Temperature and step height dependence. *Acta Mater.* **58,** 4182–4190 (2010).

Acknowledgements

This research was supported by the National Science Foundation through a CAREER Award #DMR-1056293. We thank S. Terrab (University of Colorado Boulder) for technical expertise and project support. We are also grateful to V. Vitek for critical reading of our manuscript and insightful comments. The authors also thank the support of the staff and facilities at the Penn Nanoscale Characterization Facility at the University of Pennsylvania. This work was performed, in part, at the Center for Integrated Nanotechnologies, a US Department of Energy, Office of Basic Energy Sciences user facility. Sandia National Laboratories is a multi-programme laboratory managed and operated by Sandia Corporation, a wholly owned subsidiary of Lockheed Martin Corporation, for the US Department of Energy's National Nuclear Security Administration under contract DE-AC04-94AL85000.

Author contributions

L.Y.C. and D.S.G. designed the experiments. L.Y.C. implemented the low-temperature testing set-up. L.Y.C., M-r.H. and J.S. conducted mechanical experiments and material characterization. G.R. synthesized the materials and conducted material characterization. L.Y.C. and D.S.G. developed the analytical model and performed analysis of the data. D.S.G. supervised the work. L.Y.C. and D.S.G. wrote the initial manuscript with input from all authors. All authors contributed to discussion of the results, provided input on the manuscript, and approved the final version.

Additional information

Supplementary information is available in the online version of the paper. Reprints and permissions information is available online at www.nature.com/reprints. Correspondence and requests for materials should be addressed to D.S.G.

Competing financial interests

The authors declare no competing financial interests.

Methods

Sample synthesis and characterization. Single-crystalline Pd NWs were grown by thermal evaporation at 1,200 °C onto (001)-$SrTiO_3$ or (0001)-Al_2O_3 substrates at elevated temperature under ultrahigh vacuum conditions. Further details of the growth procedure and mechanism are documented elsewhere[12]. The orientation was confirmed by electron diffraction analysis on at least ten NWs with diameters $30 < d < 150$ nm from each substrate before testing. The bottom-up growth at near-equilibrium conditions resulted in distinct surface facets, and the NWs showed no evidence of taper or visible roughness on the surfaces (Fig. 1a). High-resolution scanning transmission electron microscopy (STEM) verified the absence of a native oxide layer on the NWs. As both high temperature (>1,000 K) and oxygen partial pressure are required to form oxide layers on Pd (ref. 31), these NWs were expected to remain oxide-free during testing at elevated temperatures. For Pd NWs grown on the $SrTiO_3$ substrate (35% of entire data set), TEM imaging showed no visible pre-existing defects such as dislocations or vacancy clusters (Fig. 1b). For the remaining NWs grown on Al_2O_3, about half of the specimens examined had stacking faults (~30% of entire data set) along the axis, whereas the remainder were defect-free. Because the stacking fault is along the NW axis, its resolved shear stress is zero. Postmortem imaging in the TEM confirmed that the stacking faults remained in the NW even after fracture, and the nucleation strength distributions from data sets containing defect-free NWs and those containing stacking faults were not statistically distinct (see Supplementary Information for full analysis).

Tensile testing and temperature control. Individual NWs were harvested using a nanomanipulator directly from the growth substrate and attached onto the microelectromechanical systems (MEMS) tensile testing stage using Pt-containing electron beam-induced deposits (EBID; Fig. 1c). The stress–strain response during tensile loading was measured by tracking the displacements of the load cell and actuator (Fig. 1d) using digital image correlation. These displacements were tracked either by EBID fiducial markers placed near the sample and on the grips for SEM images or by comb features under the optical microscope[44]. Although the compliance of the EBID grips is known to affect the apparent strain measurement during tensile testing (which is corrected for), the compliance does not influence the load—and therefore strength—measurements that are the focus of this study[33]. The MEMS stage was set in a ceramic electronics package that enabled easy transport between SEM and optical set-ups as well as connection to an external power supply for operating the actuator. Owing to the low thermal mass, the stage could be heated or cooled uniformly. The package within the cryostat was thermally coupled to the heat exchanger for the cryogen (LN_2; Fig. 1e). Elevated temperatures up to 475 K were achieved with a cartridge heater connected to a PID temperature controller. The temperature reported at the sample was measured from a thermocouple attached to the tensile stage substrate. Pd NWs were tested at strain rates in the range of 10^{-5} s^{-1} to 10^{-3} s^{-1} and nominal temperatures from 77 to 475 K. Further details of the set-up, including temperature control and stability, can be found in ref. 44.

***In situ* TEM experiments—set-up.** Similar to the above manipulation procedure, individual Pd NWs were aligned and mounted on a MEMS fabricated push-to-pull (PTP) device[33] (Fig. 2a). A PI-95 TEM PicoIndenter from Hysitron[45] was then used to push the semicircle head of the PTP device with a diamond flat punch indenter at a constant displacement rate of 4 nm s^{-1}, pulling the bridged Pd NW in tension. Experiments were performed in a JEOL 2100 TEM. Load and displacement data were recorded and converted to the stress–strain response of Pd NWs based on a procedure similar to refs 33,44.

The resolution of the recorded load displacement signals was <0.2 μN and <1.0 nm, respectively. The spring constant of empty PTP device, that is, the four springs loaded in parallel with the tested NW, was measured after NW fracture. The force applied to the NW was thus determined by subtracting the elastic force of the PTP device from the total load. The cross-section of the NW was approximated as a circle, with the diameter taken as the average of projective widths with the specimen holder tilted at 0° and 30°. The initial gauge length of the NW was measured by SEM as the distance between the two Pt grips. The elongation of the NW was considered to be uniform before fracture and simply equal to the displacement of indenter, as the compliance of Pt grips has been shown to be negligible for the NW diameters tested by *in situ* TEM (refs 31,33).

References

44. Murphy, K. F., Chen, L. Y. & Gianola, D. S. Effect of organometallic clamp properties on the apparent diversity of tensile response of nanowires. *Nanotechnology* **24,** 235704 (2013).
45. Minor, A. M. *et al.* A new view of the onset of plasticity during the nanoindentation of aluminium. *Nature Mater.* **5,** 697–702 (2006).